3D Mechanical Analysis of a High-Curvature Superconducting Dipole

E. Bianchi, A. Dellacasagrande, S. Farinon, E. Felcini, A. Gagno, L. Gentini, I. Georgiadis, E. O. Kavoura, C. Kokkinos, A. Pampaloni, D. Perini, M. Prioli, M. Pullia, L. Rossi, C. Santini, and R. U. Valente

***Abstract*—The Superconducting Ion Gantry (SIG) project, developed in collaboration with INFN, CERN, CNAO, MedAustron and FEAC Engineering, aims to improve cancer treatment by creating compact and lightweight ion gantries. These systems allow for precise, non-coplanar irradiation while reducing damage to surrounding healthy tissues. A key element of this project is a 4 T curved superconducting dipole magnet, made with Nb-Ti Rutherford cables, featuring a 1.65 m curvature radius and an 80 mm aperture, designed for a 430 MeV/u carbon ion gantry. This study addresses the mechanical challenges of the magnet's curvature, maintained by two curved steel clamps, and the use of an indirect cooling system. To test the design and assembly process, a 30° demonstrator is being developed as a step toward the final 45° dipole. Building on previous 2D mechanical studies of the SIG curved dipole, this work presents a 3D FEM analysis of the magnet support structure. The vertical preload system aims to maximize the contact between the coil, collars, and yoke, evaluated through the percentage of elements in contact during assembly, cooldown, and energization. At the coil ends, the longitudinal preload system provides restraint and prevents additional movements during powering. All stresses remain within allowable limits, supporting the development of a design compatible with indirect cooling.**

***Index Terms*—Accelerator dipoles, superconducting magnets, magnets for medical systems, mechanical systems.**

Received 13 October 2025; revised 9 February 2026; accepted 9 February 2026. Date of publication 23 February 2026; date of current version 19 March 2026. *(Corresponding author: E. Bianchi.)*

E. Bianchi, S. Farinon, and A. Gagno are with the Istituto Nazionale di Fisica Nucleare Sezione di Genova, 16146 Genova, Italy (e-mail: emma.bianchi@ge.infn.it).

A. Dellacasagrande is with the Istituto Nazionale di Fisica Nucleare Sezione di Genova, 16146 Genova, Italy, and also with Università degli Studi di Genova, 16146 Genova, Italy.

E. Felcini and M. Pullia are with the Centro Nazionale di Adroterapia Oncologica, 27100 Pavia, Italy.

L. Gentini and D. Perini are with CERN, 1211 Geneva, Switzerland.

I. Georgiadis, E. O. Kavoura, and C. Kokkinos are with the FEAC Engineering P.C., 26442 Patras, Greece.

A. Pampaloni is with the Istituto Nazionale di Fisica Nucleare Sezione di Genova, 16146 Genova, Italy, and also with Sapienza Università di Roma, 00185 Roma, Italy.

M. Prioli, C. Santini, and R. U. Valente are with the Istituto Nazionale di Fisica Nucleare, Laboratorio Acceleratorie Superconduttività Applicata, 20090 Milano, Italy.

L. Rossi is with the Istituto Nazionale di Fisica Nucleare, Laboratorio Acceleratori e Superconduttività Applicata, 20090 Milano, Italy, and also with Università degli Studi di Milano, 20122 Milano, Italy.

Color versions of one or more figures in this article are available at https://doi.org/10.1109/TASC.2026.3664830.

Digital Object Identifier 10.1109/TASC.2026.3664830

TABLE I
MAIN PARAMETER OF THE MAGNET

Parameters	SIG demonstrator
Bore field	4 T
Current	2793 A
Peak field	4.38 T
Margin on loadline	21.5%
Operating temperature	5 K
Bore diameter	80 mm
Mechanical length	∼ 870 mm
Iron yoke radius	∼ 200 mm
Number of layers	2
Number of blocks per quadrant	4+3
Number of turns per quadrant	35(10+12+9+4), 43(15+18+10)
Radius of curvature	1.65 m
Angular sector	30°
Field ramp rate	0.4 T/s

I. INTRODUCTION

THE SIG project [1] is part of the EuroSIG European collaboration [2], [3], [4], [5], [6], which seeks to create more compact, lightweight, and cost-effective ion gantry systems for hadron therapy [7], [8], [9]. One of the main objectives is to design and build a 4 T curved superconducting dipole magnet using NbTi $cos\theta$ coils, with a curvature radius of 1.65 m. The main parameters of the magnet are summarized in Table I. To test the feasibility of the proposed design and manufacturing process [10], [11], a smaller 30° demonstrator will be constructed before moving onto the full 45° sector prototype. Since the dipole operates with a ramp rate of 0.4 T/s, it will experience significant AC losses, which require an efficient cooling strategy. For safety reasons and to allow rotational movement, the magnet cannot be cooled in a liquid helium bath. Therefore, the final 45° prototype will adopt an indirect cooling system, based on conduction cooling through a cryocooler or forced-flow refrigerated gas.

Indirect cooling requires good thermal contact across the interfaces between coil, collars, and yoke. These contacts may be reduced by differential thermal contractions during cooldown and by Lorentz forces during operation, so an adequate assembly preload is essential. In conventional straight magnets, this preload is applied using a press. However, the large in-plane dimension imposed by the curvature exceeds the available press capacity, and a press-free preload solution must be adopted. Previous activities within the SIG program focused on the manufacturing strategy and the optimization of the 2D cross-section [10], [11], [12], [13], [14], while the three-dimensional behavior

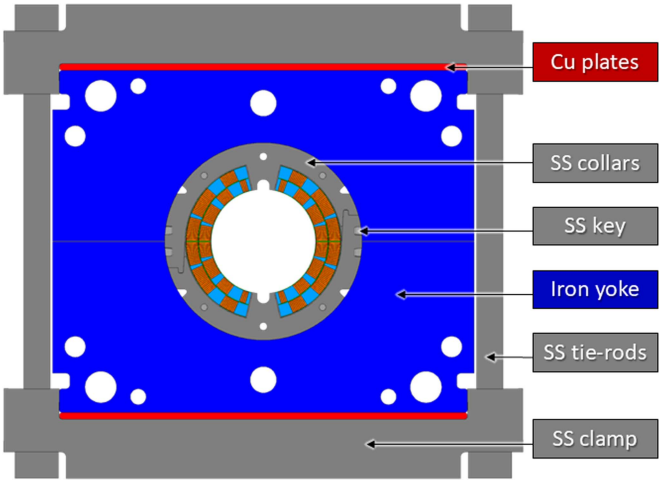

Fig. 1. Optimized 2D cross-section showing the main magnet components.

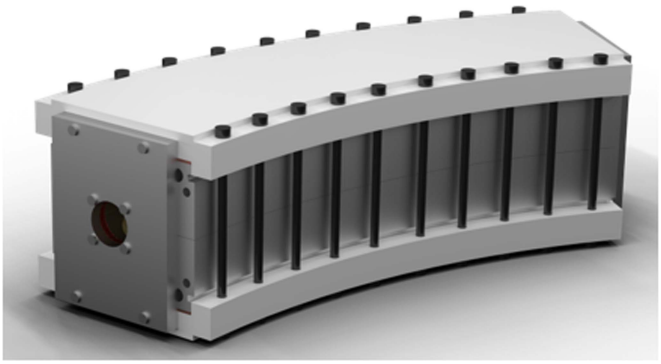

Fig. 2. 3D view of the magnet showing the curved clamp and the overall vertical preload system.

of the curved structure and the application of preload in this configuration still required further assessment. The present work addresses these aspects through a dedicated 3D FEM analysis of the 30° demonstrator. Although the magnet will be tested in a helium bath, the design is conceived to remain compatible with future conduction-cooling solutions. The preload systems are therefore defined to maximize the contact between components, and its evolution during assembly, cooldown, and energization is evaluated through the percentage of elements in contact, together with the verification of structural limits.

II. Overview of the Magnet Structure

An optimized 2D cross-section [14] (Fig. 1) was used as the basis for the 3D mechanical models. The magnet features laminated SS (Stainless Steel) collars with a designed interference between pole and coil (0.2 mm) to apply the required preload, keeping the coil in compression during operation. The load is maintained by SS keys inserted in the collar slots. A laminated iron yoke surrounds the collars, split horizontally and serving only a magnetic function.

The vertical preload system (Fig. 2) consists of a curved SS clamp and ten pairs of SS M20 tie rods. The number and diameter of the tie rods were optimized through a dedicated 3D sector model described in section III. A copper plate was placed between the clamp and the yoke to homogenize the temperature across the yoke laminations.

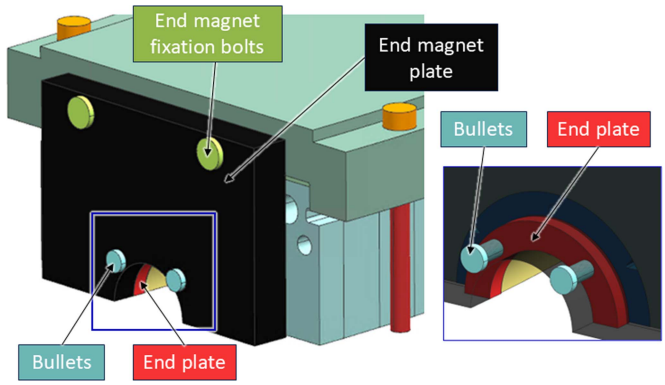

Fig. 3. Detail of the longitudinal preload system.

TABLE II
Mechanical Properties

Materials	σ limit* @ RT [MPa]	σ limit* @ 5 K [MPa]	E @ RT [GPa]	E @ 5 K [GPa]	ν	α [mm/m]
NbTi conductor	120	120	15	20	0.3	4.0
G10 wedge	214	413	25	27.5	0.3	2.5
Cu plate	270	340	110	110	0.3	3.1
SS collar, clamp tie_rod	350	1150	191	210	0.28	2.8
Armco yoke	230	720	204	225	0.28	2.0

*σ limit degradation for conductors, yield for other materials.

The longitudinal preload system (Fig. 3) includes an end magnet plate bolted to the clamp. The preload on the coil can be finely tuned using bullets acting on the red plate, which distributes the load uniformly on the coil. This system was designed and analyzed in a separate 3D model developed by FEAC engineering and described in section IV.

III. Ansys 3D Sector Model and Results

The 3D finite element analyses were performed using ANSYS Mechanical APDL 2024 R2 [15], using SOLID186 elements and flexible-to-flexible contacts for all sliding interfaces modeled with CONTA174 and TARGE170, assuming a friction coefficient of 0.2. The final mesh consisted of 697758 nodes and 834280 elements.

An elastic material model was employed, with material properties specified in Table II [16], [17], [18].

The simulation followed the same three-step procedure adopted in the 2D model [13]: assembly, cooldown, and energization. During assembly, preload was generated by activating all contact pairs with predefined interferences of 0.12 mm between the collar pole and the coil and 0.15 mm between the tie-rods and the clamps (Fig. 4), as defined in the 2D model [13]. Cooldown was simulated by applying a uniform temperature

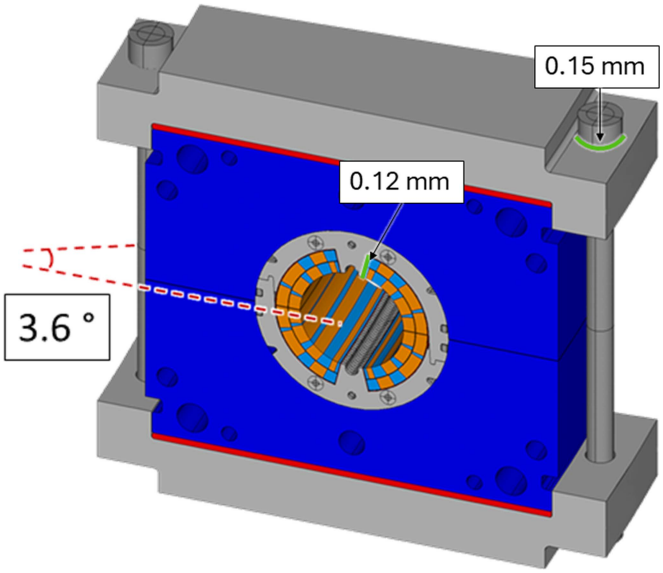

Fig. 4. 3D fem model of 3.6° sector, highlighting the contact regions where the assembly interferences are applied (shown on one quarter of the model for clarity).

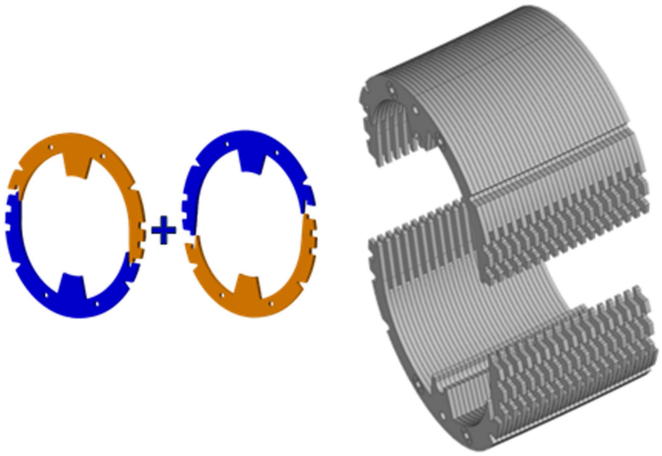

Fig. 5. Detail of the collars showing the geometric asymmetry and the modeling of the individual laminations.

decrease down to 5 K. In the final step, Lorentz forces were imported from a separate electromagnetic ANSYS simulation sharing the same geometry and mesh as the mechanical model, enabling a direct node-by-node force transfer. The model in Fig. 4 represents the smallest repeatable sector, including a tie-rod pair: 3.6° (35 collar pairs) out of the 36° magnet length. Curved components were generated by extruding the 2D cross-section [14] along a 1.65 m radius. Collars were modeled as individual laminations to capture the effect of lamination on contact distribution and to account for their asymmetry along the magnet length (Fig. 5), while other curved components, including the yoke, were represented as monolithic parts. Since only a sector was modeled, boundary conditions were applied to the nodes of the end faces. Cyclic symmetry could not be applied, so two limiting configurations were considered (Fig. 6): an under-constrained case, with free circumferential displacement of the end-face nodes, and an over-constrained case, where circumferential displacements of the end-face nodes were restrained. In both configurations, thermal contraction was left free. The actual behavior of the full magnet is expected to lie between these two extremes.

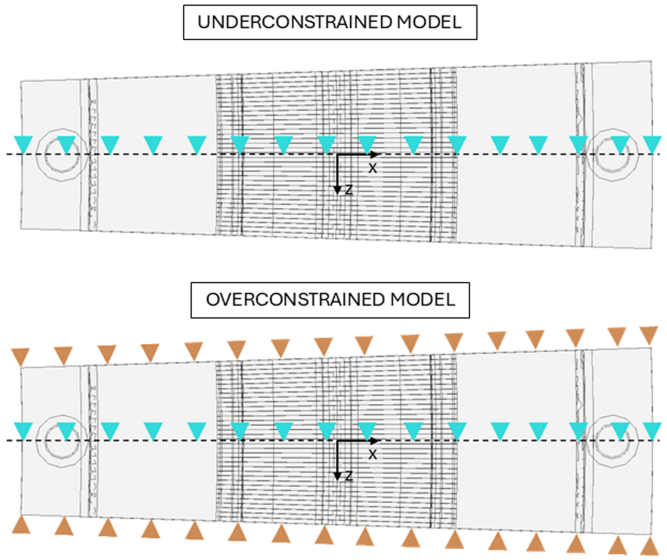

Fig. 6. Top view of the applied boundary conditions. The upper image shows the under-constrained configuration, with the end-face nodes free in the circumferential direction. The lower image shows the over-constrained configuration, where circumferential displacements of the end-face nodes are restrained. Symmetry constraints are applied at the mid-plane to prevent rigid body motion.

TABLE III
COMPARISON OF VON MISES STRESS PEAKS FOR UNDERCONSTRAINED AND OVERCONSTRAINED MODELS

	Step	Underconstrained model	Overconstrained model
σ_{VM} conductors [MPa]	1	37	34
	2	75	64
	3	75	65
σ_{VM} wedge [MPa]	1	49	45
	2	98	82
	3	99	84
σ_{VM} Cu plate [MPa]	1	34	31
	2	39	103
	3	46	106
σ_{VM} collar [MPa]	1	235	235
	2	152	122
	3	208	220
σ_{VM} yoke [MPa]	1	68	65
	2	66	152
	3	82	143
σ_{VM} clamp [MPa]	1	119	122
	2	104	330
	3	115	327
σ_{VM} tie-rod [MPa]	1	142	149
	2	154	264
	3	170	280

Table III presents the maximum von Mises stress values for key components in both the under-constrained and over-constrained models, across the three simulation steps: assembly, cooldown, and energization. Stress levels during assembly are

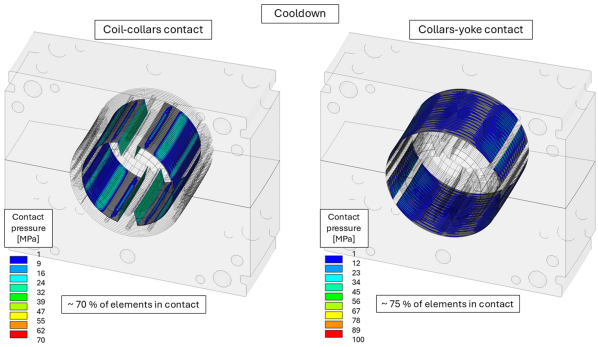

Fig. 7. Pressure map (MPa) and % of elements in contact between coil–collar and collar–yoke at the end of the cooldown (underconstrained model).

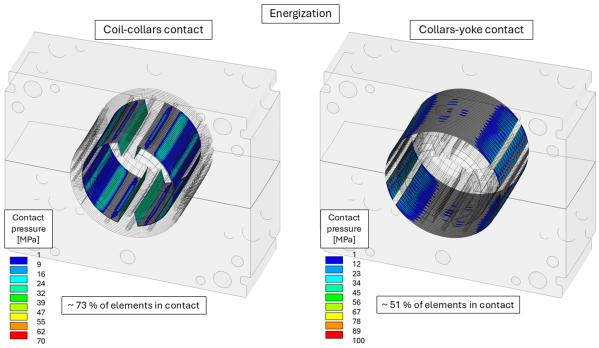

Fig. 8. Pressure map (MPa) and % of elements in contact between coil–collar and collar–yoke at the end of the energization (underconstrained model).

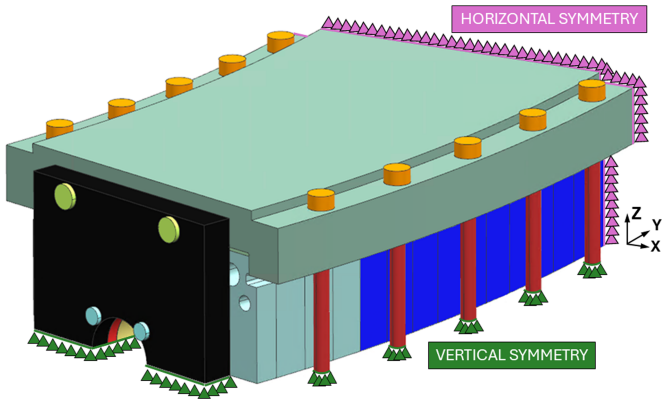

Fig. 9. Symmetry constraints applied on the axial and midplane planes of the magnet in the full length model.

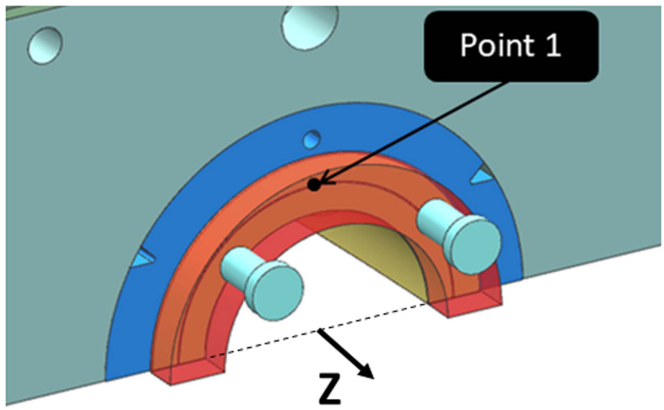

Fig. 10. Point in the middle of the Coil-End chosen for the trade-off analysis.

nearly identical. Differences become evident during cooldown, due to thermal contraction. Components with a high thermal contraction coefficient and significant thickness along the direction of the additional constraints, such as the clamp and copper plates, show a marked increase in stress in the overconstrained model. Laminated components, like the collars, behave similarly in both models. The yoke also shows significant stress variation in the simulation; however, since the actual yoke will be laminated, its behavior is expected to resemble that of the collars, with limited stress variation. Nevertheless, all stress values remain safely below material yield limits.

In Fig. 7 and Fig. 8, the contact distribution at the coil–collar and collar–yoke interfaces are shown, for both cooldown and energization. The results refer to the under-constrained model only, since the distributions are practically identical in both models. Compared to the 2D case, the 3D simulation shows lower initial contact percentages due to the coarser mesh imposed by computational limitations. The contact between the coil and the collars remains about 70% after both cooldown and energization, indicating stable mechanical behavior. For the collar–yoke interface, the percentage decreases from 75% after cooldown to 50% after energization. Since the demonstrator will operate in liquid helium, the objective at this stage is to maximize the extent and continuity of the interfaces within structural limits. The resulting contact distribution therefore represents a mechanical starting point for future thermo-mechanical investigations.

IV. SIMCENTER 3D Full Length Model and Results

The 3D finite element analyses were performed using SIEMENS [19], using mainly CHEXA8 elements and flexible-to-flexible contacts for all sliding interfaces, assuming a friction coefficient of 0.2. The final mesh consisted of 283804 nodes and 311588 elements. An elastic material model was employed, with the same material properties used in the sector model (Table II). The full-length model was built following the same steps as the sector model. To reduce computational effort, some geometric simplifications were introduced. The collar asymmetry was removed so that only one quarter of the magnet could be modeled. The collars were also represented as a single solid instead of individual laminations, like the other components. Symmetry constraints were applied to the axial and midplane symmetry planes, as shown in Fig. 9.

A trade-off analysis was performed by varying the interference between the bullets and the end plates from 0.1 mm to 0.5 mm (where plastic deformation of the bullets occurs). The corresponding longitudinal displacement of a point located at mid coil-end (Fig. 10) is reported in Fig. 11. The key observation is that the transition from cooldown to energization does not introduce additional displacement, indicating that the assembly

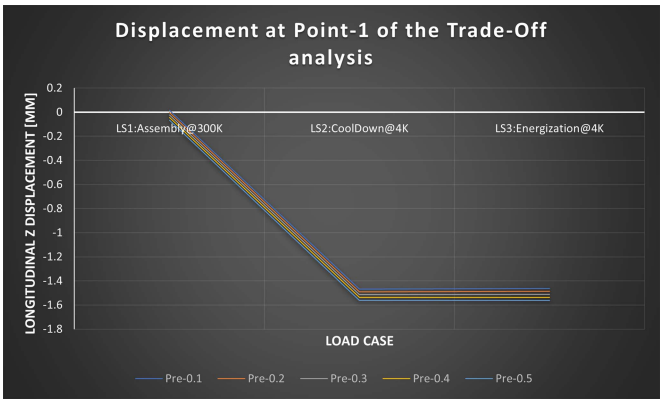

Fig. 11. Displacement at point 1 for different Bullet pretension.

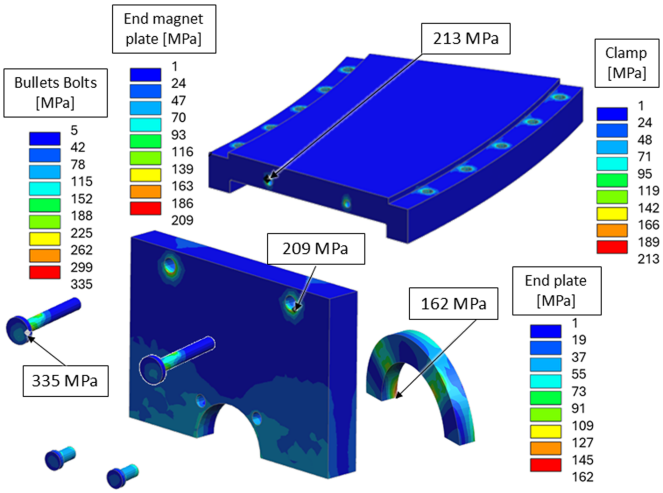

Fig. 12. Von Mises stress map (MPa) in the main components of the longitudinal preload system after energization, with peaks highlighted.

remains stable during energization. Based on this analysis, an interference of 0.2 mm was selected as a suitable value.

The von Mises stress distributions corresponding to this configuration are shown in Fig. 12 for the most critical step, the energization. Only this step is reported, since the other load steps exhibit significantly lower stress levels. Even at energization, all components remain below their structural limits.

V. Conclusion

The two 3D models provided a comprehensive understanding of the SIG magnet's mechanical behavior under operating conditions. The short model allowed the correct sizing of the vertical preload system, consisting of ten pairs of M20, and was used to verify the most critical interfaces. The full-length model enabled the design of the longitudinal preload system, where a trade-off analysis identified 0.2 mm as the optimal bullet interference. In both models, all components remained within structural limits throughout all operating steps.

References

[1] M. Prioli et al., "Design of a 4 T curved demonstrator magnet for a superconducting ion gantry," *IEEE Trans. Appl. Supercond.*, vol. 33, no. 5, Aug. 2023, Art no. 4400505, doi: 10.1109/TASC.2023.3244523.

[2] L. Rossi et al., "A European collaboration to investigate superconducting magnets for next generation heavy ion therapy," *IEEE Trans. Appl. Supercond.*, vol. 32, no. 4, Jun. 2022, Art no. 4400207, doi: 10.1109/TASC.2022.3147433.

[3] "Website of HITRIplus (heavy ion therapy research integration)," 2022. [Online]. Available: https://www.hitriplus.eu/

[4] "Website of IFAST (innovation fostering in accelerator science and technology)," 2022. [Online]. Available: https://ifast-project.eu/home

[5] L. Rossi et al., "Magnet technology and design of superconducting magnets for heavy ion gantry for hadron therapy," in *Proc. 14th Int. Part. Accel. Conf.*, Geneva, Switzerland, 2023, pp. 4923–4926. [Online]. Available: https://indico.jacow.org/event/41/contributions/2869

[6] M. Prioli et al., "Superconducting magnets technology for a European heavy ion gantry," in *Proc. 15th Int. Part. Accel. Conf.*, Geneva, Switzerland, 2024, pp. 1880–1884. [Online]. Available: https://indico.jacow.org/event/63/contributions/3091

[7] T. Haberer et al., "The Heidelberg ion therapy center," *Radiother. Oncol.*, vol. 73, pp. S186–S190, 2004.

[8] Y. Iwata et al., "Design of a superconducting rotating gantry for heavyion therapy," *Phys. Rev. Special Topics Accel. Beams*, vol. 15, no. 4, 2012, Art. no. 044701.

[9] M. G. Pullia et al., "Gantries for carbon ions," *Health Technol.*, vol. 14, pp. 973–983, Apr. 2024, doi: 10.1007/s12553-024-00870-7.

[10] M. Prioli et al., "First winding trial for the superconducting ion gantry (SIG) dipole demonstrator magnet," *IEEE Trans. Appl. Supercond.*, vol. 34, no. 5, pp. 1–5, Aug. 2024, doi: 10.1109/TASC.2024.3361440.

[11] M. Prioli, et al., "Manufacturing of the EuroSIG dipole demonstrator magnet for hadrontherapy," *IEEE Trans. Appl. Supercond.*, early access, 2026, doi: 10.1109/TASC.2026.3664351.

[12] F. Levi et al., "Mechanical design of the 4 T curved demonstrator dipole for the SIG gantry," *IEEE Trans. Appl. Supercond.*, vol. 34, no. 5, Aug. 2024, Art no. 4400505, doi: 10.1109/TASC.2023.3333262.

[13] E. Bianchi et al., "Consolidated 2D mechanical design and preliminary 3D design phase of the superconducting ion gantry (SIG) dipole for hadrontherapy," *IEEE Trans. Appl. Supercond.*, vol. 35, no. 5, Aug. 2025, Art no. 4001105, doi: 10.1109/TASC.2024.3520080.

[14] M. Prioli et al., "Eurosig framework - conceptual design report of the superconducting ion gantry (SIG) dipole demonstrator magnet," Apr. 2025, doi: 10.15161/oar.it/211921.

[15] ANSYS website, 2025. [Online]. Available: https://www.ansys.com/

[16] "Data presented in EuroCirCol-P1-WP5, 2016. [Online]. Available: https://www.lnf.infn.it/sis/preprint/getfilepdf.php?filename=INFN-22-01-GE.pdf

[17] "Characterization of low-carbon steel for high-field accelerator magnets, 2020. [Online]. Available: https://indico.cern.ch/event/892944/attachments/1994390/3333553/structural_limits_ARMCO_and_MQXF-v5.pdf

[18] G. Vallone, E. Anderssen, B. Bordini, and P. Ferracin, "A review of the mechanical properties of materials used in Nb_3Sn magnets for particle accelerators," *IEEE Trans. Appl. Supercond.*, vol. 33, no. 5, Aug. 2023, Art. no. 4002806, doi: 10.1109/TASC.2023.3248544.

[19] Siemens website, 2025. [Online]. Available: https://www.sw.siemens.com/en-US/